RAPID COMMUNICATION





Slow sintering in garnet-containing Y and Gd zirconate-aluminate mixtures for thermal barrier coatings

Department of Chemical Engineering and Materials Science, University of Minnesota, Minneapolis, Minnesota, USA

Correspondence

David L. Poerschke, Department of Chemical Engineering and Materials Science, University of Minnesota, Minneapolis, MN, USA. Email: poerschke@umn.edu

Funding information

NASA, Grant/Award Number: 80NSSC21C0071; NSF REU program, Grant/Award Number: DMR-1852044; University of Minnesota MRSEC NSF, Grant/Award Number: DMR-2011401; NNCI, Grant/Award Number: ECCS-2025124

Abstract

Mixtures of rare-earth zirconates and aluminates containing Y or Y + Gd that form a two-phase garnet–fluorite mixture exhibit much slower sintering than pure fluorite at 1400° C. An equivalent Y-free, Gd-containing composition that forms a perovskite aluminate instead of garnet showed faster densification after the metastable garnet decomposes. At 1500° C, the Y-free sample also showed the fastest initial sintering rate, whereas there was more divergence in the sintering rate for the samples containing Y + Gd. The zirconate–aluminate with equimolar Y + Gd shows the slowest densification at 1500° C and retains $\sim 25\%$ porosity after 250 h. The results highlight possibilities for designing compliant thermal barrier coatings that can retain significant porosity at 1400° C or higher.

KEYWORDS

aluminates, rare-earth oxides, sintering, thermal barrier coatings, zirconates

1 | INTRODUCTION

Thermal and environmental barrier coatings (TBC and EBC used separately, or as an integrated T/EBC) protect alloy and ceramic composite components to improve turbine engine performance and efficiency. Their performance is determined by a combination of thermophysical properties, including thermal conductivity (κ), coefficient of thermal expansion (CTE), phase and microstructure stability, compliance, and toughness.^{1–3} Deficiencies in the property combinations for individual materials can be mitigated through careful architecture design. For instance, advanced TBCs for Ni-superalloys combine an inner layer of tough, but metastable, t' yttria stabilized zirconia (YSZ) with an outer layer of a rare-earth (RE) zirconate with lower κ and improved phase stability, but

lower fracture toughness, compared to YSZ.^{4,5} Controlling the through-thickness porosity to balance toughness, thermal stress generation, and thermal conductivity can further improve performance.⁶ Likewise, proposed T/EBC architectures for SiC-based composites combine RE disilicate layers, which minimize the CTE mismatch with an outer layer of a segmented or porous RE monosilicate, aluminate, zirconate, or hafnate that is more volatilization resistant.^{7,8}

The ability of these architectures to resist sintering and coarsening is critical to enable higher coating surface temperatures, since sintering of porous coatings induces sintering strains and reduces strain compliance. The ordered RE zirconate and hafnate pyrochlore and δ -phase offer somewhat slower sintering than YSZ, but disordering to the defect fluorite structure (F) at higher

This is an open access article under the terms of the Creative Commons Attribution-NonCommercial-NoDerivs License, which permits use and distribution in any medium, provided the original work is properly cited, the use is non-commercial and no modifications or adaptations are made.

© 2023 The Authors. Journal of the American Ceramic Society published by Wiley Periodicals LLC on behalf of American Ceramic Society.

15512916, 2023, 8, Downloaded from https://ceramics.onlinelibrary.wiley.com/doi/10.1111/jace.19121 by UNIVERSITY OF MINNESOTA 170 WILSON LIBRARY, Wiley Online Library on [18/08/2023]. See the Terms and Conditions (https://onlinelibrary.wiley.com/term

and-conditions) on Wiley Online Library for rules of use; OA articles are governed by the applicable Creative Commons License

FIGURE 1 Calculated 1500°C isothermal sections containing the Gd- and Y-based endmembers and illustrating the change in equilibria when the garnet aluminate is destabilized upon increasing the rare-earth (RE) cation radius.

temperatures can reduce this benefit. Indeed, experiments show that initially porous coatings of δ -Yb₄Hf₃O₁₂ used as part of a multilayer T/EBC system sinter unacceptably quickly at 1500°C. 10 This understanding motivates the development of new coating materials with improved sintering resistance at high temperatures.

This report demonstrates that the addition of alumina to stabilize a RE aluminate garnet (RE₃Al₅O₁₂, REAG or G) in equilibrium with the RE zirconate fluorite significantly reduces the sintering rate at 1400°C compared to singlephase fluorite. The approach is motivated by the low ternary solubility of the two phases^{11,12} and the knowledge that full occupation of the three distinct cation sites in garnet without introducing anion vacancies could reduce cation diffusivity. The results also show that increasing the RE cation radius from Y³⁺ to Gd³⁺ destabilizes garnet in favor of the RE perovskite (REAlO₃, REAP or P). This transition is accompanied by a marked increase in the sintering rate, consistent with results showing that GdAP, Gd-zirconate, and mixed GdAP and zirconate reach full theoretical density with extended sintering.¹³ This comparison demonstrates that the beneficial effect of the alumina addition to reduce sintering depends on the specific phase assemblage.

The compositions Al₃₀RE₃₅Zr₃₅, where the subscript denotes the atomic percentage of the cations and $RE_{35} = Gd_{35}$, $Gd_{30}Y_5$, $Gd_{17.5}Y_{17.5}$, Gd_5Y_{30} , or Y_{35} , were selected. These compositions fall on a notional tie line between the aluminate garnet and zirconate fluorite. Thermodynamic modeling using the Thermo-Calc TCOX10 database predicts that Al₃₀Y₃₅Zr₃₅ will form YAG and fluorite; however, the equilibrium assemblage for Al₃₀Gd₃₅Zr₃₅ consists of GdAP, alumina (Al₂O₃), and fluorite (Figure 1). In other words, increasing the cation size from Y³⁺ to Gd³⁺ destabilizes garnet. Thus,

the mixed Y + Gd samples capture the transition from the G + F to $Al_2O_3 + P + F$ equilibrium assemblages. However, experimental studies have shown that while the equilibrium YAG crystalizes directly during synthesis, 14 the equilibrium Al₂O₃ + GdAP assemblage is slow to develop with metastable GdAG existing for extended time at 1400°C.15 The Gd- and Y-based fluorite compositions predicted to form at equilibrium in these samples, that is, Y₃₃Zr₆₇ and Gd₃₅Zr₆₅ from the 1500°C sections, were studied for comparison.

EXPERIMENTAL PROCEDURES

Powders were synthesized by reverse coprecipitation⁷ from metal nitrate (99.9% pure, Alfa Aesar) solutions in ethanol (for Y, Gd, and Al) or distilled water (for Zr). The solutions were mixed in appropriate proportions and added dropwise to aqueous ammonium hydroxide with pH \geq 10 maintained during the precipitation. The precipitates were separated by centrifugation, washed with ethanol, dried, pyrolyzed at 1000°C, ball milled (25 Hz, 4 h, zirconia media), cold pressed into 6 mm diameter pellets, and sintered in air at 1400 or 1500°C for times totaling between 1 and 250 h. The temperatures were selected based on prospective coating temperatures for turbine engines and knowledge of GdAG metastability around 1400°C. 15 Four pellets were sintered for the shortest time. Then, one pellet was removed from the set for microstructure characterization and the remaining samples were sintered to achieve the next desired total sintering time. The mass and volume were measured to calculate the density of each pellet. Volume measurements via Archimedes method and calipers (assuming cylindrical shape) yielded similar values. The theoretical density for each composition, used to calculate relative density ($\rho_{\rm rel}$), was obtained by correlating the porosity observed in cross-sectional electron micrographs for the 50 h samples and the density measured. The quantitative porosity values used for this calibration were obtained by thresholding using the ImageJ software, and the calibration was done separately for the samples sintered at 1400 and 1500°C given the possible difference in phase equilibrium.

Powder X-ray diffraction (XRD, Rigaku MiniFlex 600, step = 0.04° , dwell time per step = 3.6 s) was used to identify the phases of the sintered powders. The XRD patterns were normalized to the (111) fluorite diffraction peak at 2θ ~30° to facilitate comparison. The pellets were polished and thermally etched for 1 h at the sintering temperature before scanning electron microscopy (SEM) analysis. Backscattered SEM (BS-SEM, Hitachi SU8230) was used to characterize the microstructures. Energy-dispersive

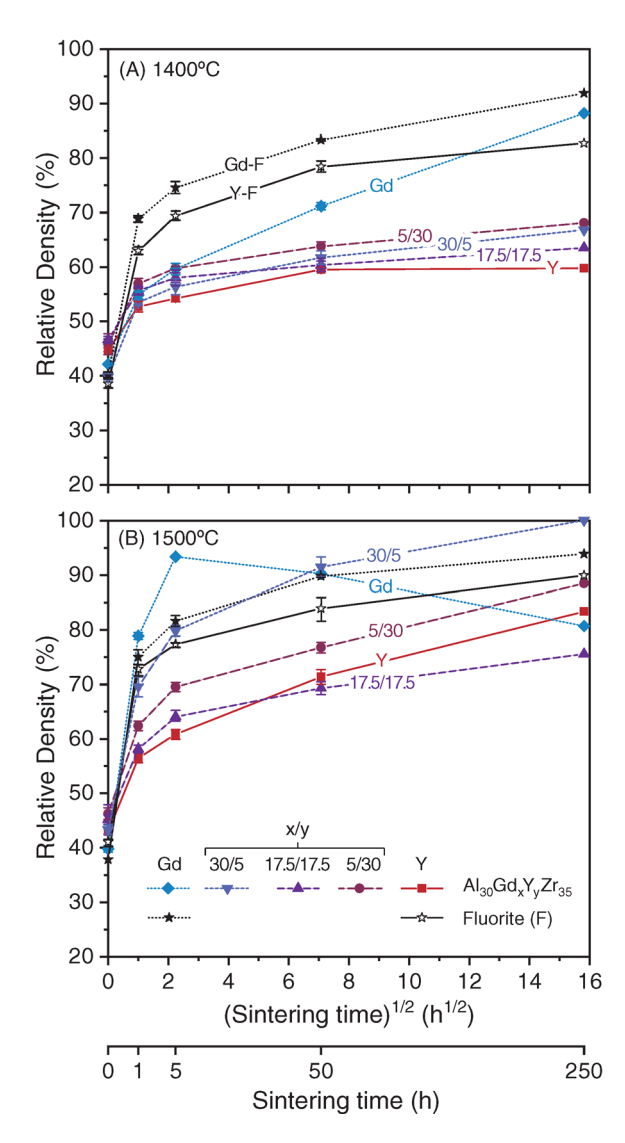


FIGURE 2 Relative density as a function of time at (a) 1400°C and (b) 1500°C. The error bars represent the standard deviation between multiple samples sintered at the same condition.

X-ray spectroscopy (EDS, Thermo Noran System 7 Spectral Imaging) assisted the phase identification.

3 | RESULTS AND DISCUSSION

Figure 2a,b shows the change in $\rho_{\rm rel}$ as a function of sintering time at 1400 and 1500°C, respectively. The as-pressed (green) relative densities fall roughly in the range of 40%–45%. The Y- and Gd-fluorites show similar densification rates, reaching $\rho_{\rm rel}$ of 80%–90% after 250 h at 1400°C and 90%–95% after 250 h at 1500°C. The implication is that although the Gd-based fluorite sinters slightly faster than the Y-based fluorite, the RE cation choice by itself does not profoundly change the sintering behavior of the same phase.

At 1400°C, $Al_{30}Y_{35}Zr_{35}$ shows sluggish sintering with ρ_{rel} increasing only slightly between 5 and 250 h, with a plateau ~60%. The mixed $Al_{30}(Gd,Y)_{35}Zr_{35}$ samples also sinter much slower than the fluorite, with final ρ_{rel} in the range of 60–70%. $Al_{30}Gd_{35}Zr_{35}$ exhibits slow initial densification after 1 h at 1400°C, but the sintering rate increases after 5 h and, after 250 h, the ρ_{rel} for the $Al_{30}Gd_{35}Zr_{35}$ exceeds 85%. In other words, the alumina addition does not suppress sintering in the Gd-based system as it does for the Y and Y + Gd materials.

Relative density and sintering time can be correlated by a power law fit with coefficients α and N (Equation 1), where ρ_0 is green density and t is sintering time. The results (Table 1) suggest that long sintering timesare required to reach full density at 1400°C for all samples except $Al_{30}Gd_{35}Zr_{35}$. The large magnitude of these predictions is due to the fact that the density plateaus later in the experiment, leading to a low sintering rate at long times in the model. $Al_{30}Gd_{17.5}Y_{17.5}Zr_{35}$ has the lowest sintering rate based on the fitting results.

$$\rho_{\rm rel} - \rho_{\rm o} = \alpha t^N \tag{1}$$

Microstructure observations (Figure 3) corroborate the density measurements. At 1400°C, the visible porosity in the Al₃₀Y₃₅Zr₃₅ and Al₃₀(Gd,Y)₃₅Zr₃₅ samples decreases only modestly between 1 and 250 h, and interconnected porosity remains even as the microstructures coarsen. The presence of large pores and low densification rates until 250 h suggest long durations of the initial sintering stage at 1400°C. Although the final densities of all the Y-containing samples are similar, the final grain sizes increase with increasing Gd content. Based on semiquantitative EDS and XRD analysis (Figure 4a), each of these samples exhibits a two-phase microstructure comprising fluorite and garnet. Conversely, much of the porosity evident in the Al₃₀Gd₃₅Zr₃₅ sample sintered for 1 h (Figure 3e) has essentially vanished after 250 h (Figure 3j), indicating the transition to the intermediate sintering stage in the same time.

The XRD data (Figure 4a) show that after 1 h at 1400° C, the Al $_{30}$ Gd $_{35}$ Zr $_{35}$ sample comprises primarily garnet and fluorite, with weak reflections indicative of a small fraction of perovskite. Over time, the relative intensities of the perovskite reflections increase while those for garnet decrease, indicating that the garnet is transforming to perovskite. Alumina, which is necessary to maintain mass balance as the metastable garnet transforms to perovskite, appears as occasional, larger grains in the microstructures beginning after 50 h. Crystalline alumina was not detected by XRD, perhaps due to the small volume fraction. The inference is that the increase in sintering coincides with destabilization of the garnet phase as the average RE³⁺ size is increased from Y³⁺ to Gd³⁺.

TABLE 1 Kinetic parameters for sintering obtained using Equation (1) and the corresponding required times expected to reach full density (t_{full}).

		1400°C			1500°C	
Composition	α	N	t _{full} (h)	α	N	t _{full} (h)
$Al_{30}Gd_{35}Zr_{35} \\$	0.123	0.231	800		a	
$Al_{30}Gd_{30}Y_5Zr_{35}$	0.136	0.123	1.8×10^{5}	0.276	0.137	190
$Al_{30}Gd_{17.5}Y_{17.5}Zr_{35} \\$	0.092	0.109	1.0×10^{7}	0.137	0.148	12 100
$Al_{30}Gd_{5}Y_{30}Zr_{35} \\$	0.112	0.124	3.4×10^{5}	0.167	0.166	1150
$Al_{30}Y_{35}Zr_{35}$	0.079	0.127	4.0×10^{6}	0.133	0.199	1540

^aDue to non-monotonic sintering behavior, fit was not performed.

At 1500°C, the aluminate-containing compositions exhibit increased densification rates and greater spread in behavior compared to 1400°C (Figure 2). In the first hour, the relative density increases for Al₃₀Y₃₅Zr₃₅, $Al_{30}Gd_5Y_{30}Zr_{35}$, and $Al_{30}Gd_{17.5}Y_{17.5}Zr_{35}$ are about half those of fluorite, Al₃₀Gd₃₀Y₅Zr₃₅ is comparable to fluorite, and Al₃₀Gd₃₅Zr₃₅ sinters faster than pure fluorite. After 1 h at 1500°C, the $Al_{30}Y_{35}Zr_{35}$ and $Al_{30}(Gd,Y)_{35}Zr_{35}$ microstructures comprise two-phase mixtures of fluorite and garnet with interconnected porosity (Figure 5a-d). Al₃₀Gd₃₅Zr₃₅ forms a mixture of fluorite, perovskite, and garnet with little visible porosity (alumina must be present to maintain mass balance but was rarely observed). The general features of these microstructures after 1 h at 1500°C are comparable to those observed after 250 h at 1400°C.

With increasing time at 1500° C, the $Al_{30}Y_{35}Zr_{35}$ and $Al_{30}(Gd,Y)_{35}Zr_{35}$ samples retain the fluorite and garnet two-phase structures (Figure 5f–i). Their sintering behaviors follow similar trajectories but with divergence in magnitude. After 250 h at 1500° C, $Al_{30}Gd_{17.5}Y_{17.5}Zr_{35}$ sinters least followed by $Al_{30}Y_{35}Zr_{35}$ and $Al_{30}Gd_5Y_{30}Zr_{35}$. In contrast, $Al_{30}Gd_{30}Y_5Zr_{35}$ surpasses fluorite and shows features of the final stage of sintering with ~100% relative density. The reason for this divergence is unclear, given that the apparent phase constitution does not change. A key result is that several of the garnet-containing samples exhibit sufficiently slower sintering than pure fluorite to likely provide benefit in a porous coating architecture.

Based on the power law fit with Equation (1), these compositions are expected to reach full density over a range of time from 10^2 to 10^4 h at $1500^{\circ} C$ (Table 1). The sintering rates of each composition inferred from this analysis exhibit the same trend at 1400 and $1500^{\circ} C$. The equimolar Y + Gd composition (Al $_{30} Gd_{17.5} Y_{17.5} Zr_{35}$) has the highest sintering resistance, whereas the Gd-rich composition (Al $_{30} Gd_{30} Y_5 Zr_{35}$) sintering is significantly accelerated as temperature increases.

The behavior of Al₃₀Gd₃₅Zr₃₅ at 1500°C is notably different. It initially sinters rapidly, reaching a peak near its

theoretical density after 5 h. The density then drops, ending with $\rho_{\rm rel}$ ~80% after 250 h. This peak and subsequent reduction in relative density coincide with the disappearance of garnet XRD reflections indicating the completion of the transformation of garnet to a mixture of perovskite and alumina between 5 and 50 h. At the same time, grain growth accelerates compared to the other samples, and the appearance of larger, rounded pores contributes to the lower relative density. These features are shown in the lower magnification inset in Figure 5j. The hypothesis is that the high densification rate of Al₃₀Gd₃₅Zr₃₅ in the early stage at 1500°C mirrors the accelerated sintering as the metastable garnet decomposes over a longer time at 1400°C. The driving force or mechanism for microstructure evolution clearly changes upon destabilization of the garnet phase, and the resulting behavior would not be advantageous for T/EBC applications.

Other reports suggest that aluminates—either on their own, or as aluminate–zirconate composites—could offer other benefits for use in T/EBCs. The garnet aluminates exhibit relatively low κ and oxygen diffusivity, which benefits their use as both thermal and environmental barriers. The lower composite CTE for the aluminate-containing materials compared to the pure zirconates also improves their suitability as top coats for T/EBC systems on refractory alloys, which have lower CTE than Ni-based alloys and require porous architectures to limit thermal stress generation at envisioned higher service temperatures. Prior work also demonstrates that aluminates and aluminate–zirconate composites offer benefits in terms of silicate deposit (CMAS) reactivity, toughness, and erosion resistance. $^{22-24}$

Finally, these results motivate exciting new directions for fundamental studies to understand how the interplay among interface energies, cation partitioning, and bulk and local defect densities and structures drives the dramatic changes in sintering behavior observed in this study. Such understanding would accelerate efforts to discover new sintering-resistant materials for high-temperature applications requiring porous ceramics.

journal

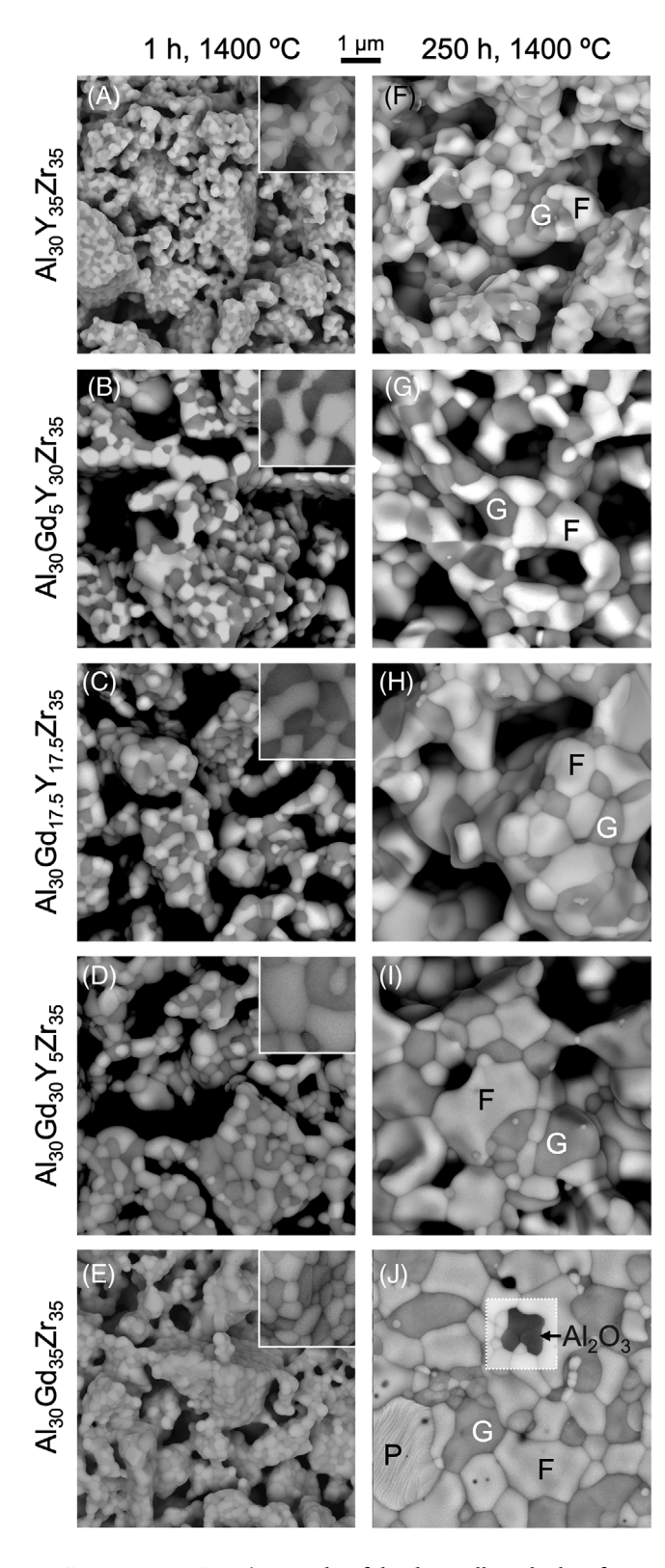


FIGURE 3 BSE micrographs of the thermally etched surfaces of the Al $_{30}$ RE $_{35}Zr_{35}$ (RE = Y or Gd) samples sintered for (A–E) 1 h and (F–J) 250 h at 1400°C. The full width of the insets in (A–E) is 1 μm . The contrast in the boxed area in (J) was adjusted to show the Al $_2$ O $_3$ against the brighter Gd-containing phases. F, fluorite; G, garnet; P, perovskite.

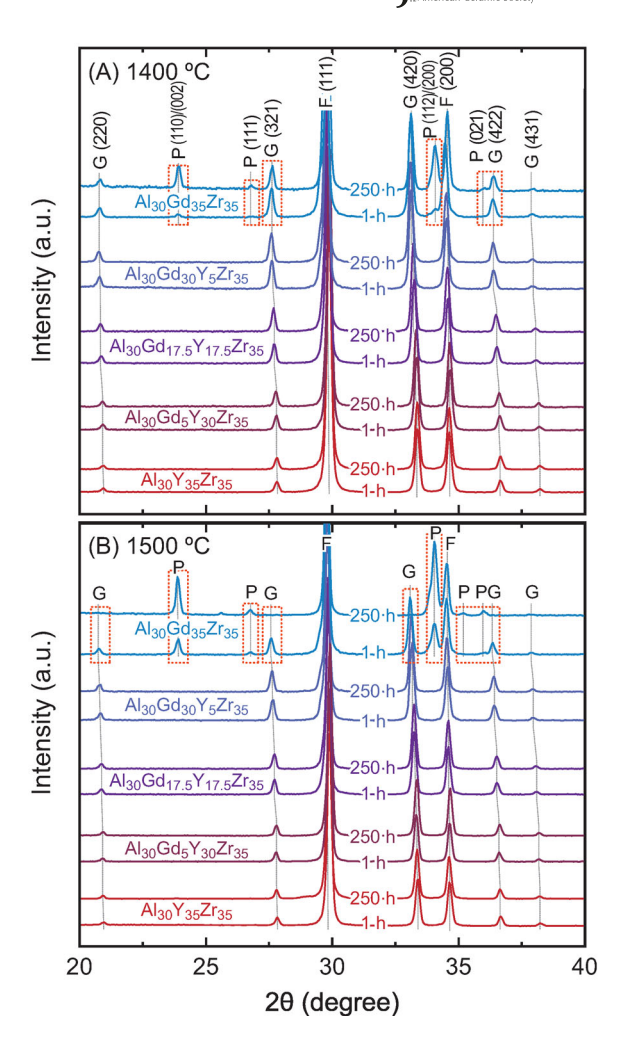


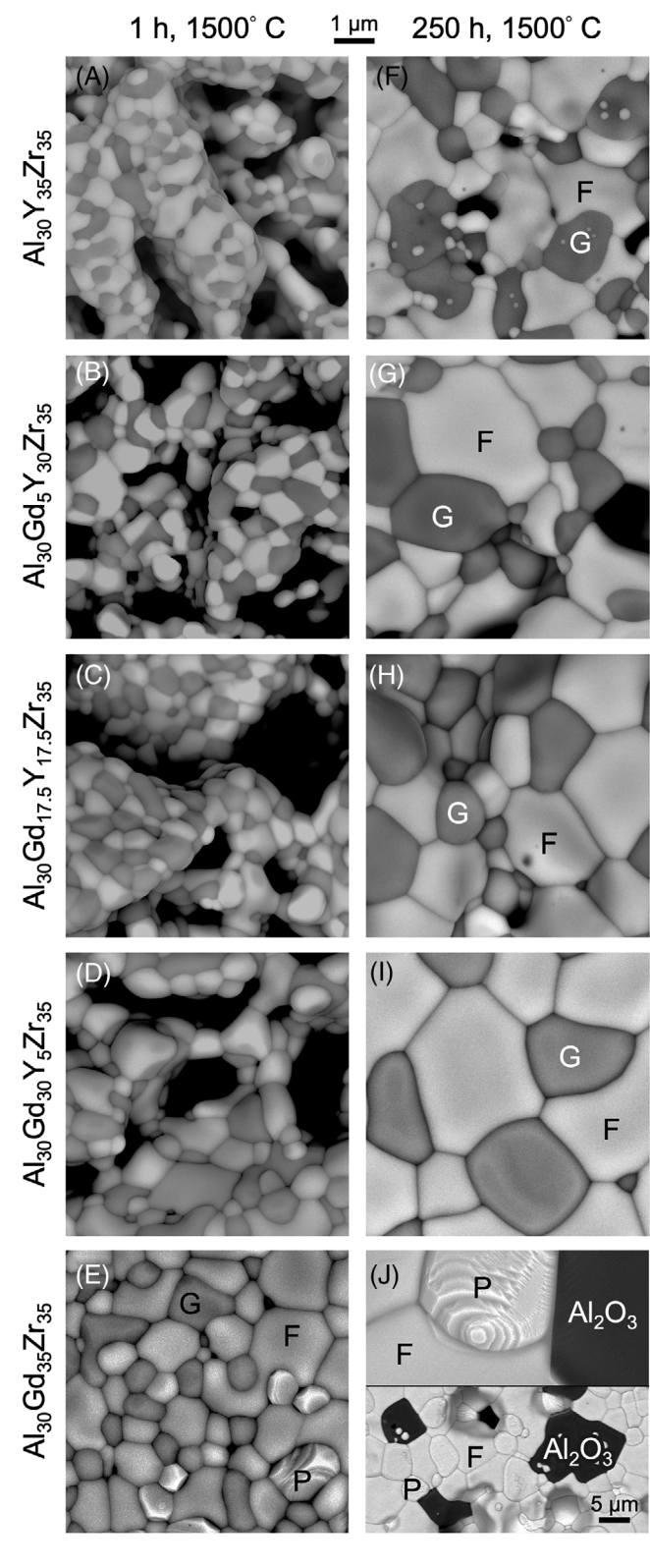
FIGURE 4 X-ray diffraction (XRD) patterns of samples sintered at (A) 1400°C and (B) 1500°C. Data from samples at intermediate times were consistent with the trends shown here. The dashed boxes indicate notable changes between 1 and 250 h. F, fluorite; G, garnet; P, perovskite.

4 | CONCLUSIONS

Two-phase microstructures containing the garnet RE aluminate in equilibrium with a RE zirconate generally have better sintering resistance than either the single-phase zirconate or a multiphase mixture containing the perovskite RE aluminate. This effect is especially clear at 1400°C, but also evident at 1500°C except for one Gd-rich, mixed RE case, which may be attributed to borderline garnet stability. The pure Y and the equimolar Y + Gd compositions exhibit the highest porosity (~40% and ~25%) after 250 h sintering at 1400 and 1500°C, respectively. For RE = Gd, the garnet phase is metastable and decomposes into perovskite and alumina accompanied by rapid densification and grain coarsening. The results suggest an advantageous route to maintain low κ and high compliance during long-term operation of a porous composite aluminate-zirconate TBC containing the garnet phase.

15512916, 2023, 8, Downloaded from https://ecramics.onlinelibrary.wiley.com/doi/10.1111/jace.19121 by UNIVERSITY OF MINNESOTA 170 WILSON LIBRARY, Wiley Online Library on [18/08/2023]. See the Terms and Conditions (https://onlinelibrary.wiley.com/terms/

-and-conditions) on Wiley Online Library for rules of use; OA articles are governed by the applicable Creative Commons License



BSE micrographs of the thermally etched surfaces of the $Al_{30}RE_{35}Zr_{35}$ (RE = Y or Gd) samples sintered for (A-E) 1 h and (F-J) 250 h at 1500°C. The scale bar at the top applies to all panels except the bottom half of (J). F, fluorite; G, garnet; P, perovskite.

ACKNOWLEDGMENTS

This research was supported primarily by NASA award number 80NSSC21C0071 monitored by Dr. Cameron Bodenschatz, in collaboration with QuesTek Innovations LLC. J.B. and N.H. were supported by the NSF REU program under Award Number DMR-1852044 and through the University of Minnesota MRSEC under Award Number DMR-2011401. Part of this work was carried out in the Characterization Facility at the University of Minnesota, which receives partial support from the NSF through the MRSEC (DMR-2011401) and the NNCI (ECCS-2025124) programs. The authors are grateful to Dr. Noriaki Arai (QuesTek Innovations LLC) for insightful discussions.

ORCID

Yueh-Cheng Yu https://orcid.org/0000-0002-2162-2728 Eeshani P. Godbole https://orcid.org/0000-0002-2685-0041

Nethmi Hewage https://orcid.org/0000-0001-7062-7114 David L. Poerschke https://orcid.org/0000-0002-6206-235X

REFERENCES

- 1. Evans AG, Clarke DR, Levi CG. The influence of oxides on the performance of advanced gas turbines. J Eur Ceram Soc. 2008;28(7):1405–19. https://doi.org/10.1016/j.jeurceramsoc.2007. 12 023
- 2. Clarke DR, Oechsner M, Padture NP. Thermal-barrier coatings for more efficient gas-turbine engines. MRS Bull. 2012;37(10):891-902. https://doi.org/10.1557/mrs.2012.232
- 3. Turcer LR, Padture NP. Towards multifunctional thermal environmental barrier coatings (TEBCs) based on rare-earth pyrosilicate solid-solution ceramics. Scr Mater. 2018;154:111–7. https:// doi.org/10.1016/j.scriptamat.2018.05.032
- Vaßen R, Traeger F, Stöver D. New thermal barrier coatings based on pyrochlore/YSZ double-layer systems. Int J Appl Ceram Technol. 2004;1(4):351-61. https://doi.org/10.1111/j.1744-7402.2004.tb00186.x
- 5. Viswanathan V, Dwivedi G, Sampath S. Multilayer, multimaterial thermal barrier coating systems: design, synthesis, and performance assessment. J Am Ceram Soc. 2015;98(6):1769-77. https://doi.org/10.1111/jace.13563
- 6. Viswanathan V, Dwivedi G, Sampath S. Engineered multilayer thermal barrier coatings for enhanced durability and functional performance. J Am Ceram Soc. 2014;97(9):2770-8. https://doi. org/10.1111/jace.13033
- 7. Poerschke DL, Van Sluytman JS, Wong KB, Levi CG. Thermochemical compatibility of ytterbia-(hafnia/silica) multilayers for environmental barrier coatings. Acta Mater. 2013;61(18):6743-55. https://doi.org/10.1016/j.actamat.2013.07.047
- Spitsberg I, Steibel J. Thermal and environmental barrier coatings for SiC/SiC CMCs in aircraft engine applications. Int J Appl Ceram Technol. 2004;1(4):291-301. https://doi.org/10.1111/ j.1744-7402.2004.tb00181.x

Iournal

- 9. Cao X, Vassen R, Stöver D, Ceramic materials for thermal barrier coatings. J Eur Ceram Soc. 2004;24(1):1-10. https://doi.org/10. 1016/S0955-2219(03)00129-8
- 10. Poerschke DL, Hass DD, Eustis S, Seward GGE, Van Sluytman JS, Levi CG. Stability and CMAS resistance of ytterbiumsilicate/hafnate EBCs/TBC for SiC composites. J Am Ceram Soc. 2015;98(1):278-86. https://doi.org/10.1111/jace.13262
- 11. Lakiza S, Fabrichnaya O, Wang C, Zinkevich M, Aldinger F. Phase diagram of the ZrO₂-Gd₂O₃-Al₂O₃ system. J Eur Ceram Soc. 2006;26(3):233-46. https://doi.org/10.1016/j.jeurceramsoc. 2004.11.011
- 12. Fabrichnaya O, Aldinger F. Assessment of thermodynamic parameters in the system ZrO₂-Y₂O₃-Al₂O₃. Int J Mater Res. 2004;95(1):27-39. https://doi.org/10.3139/ijmr-2004-0007
- 13. Wolfe DE, Schmitt MP. Thermal barrier coatings. U.S. Patent Application 2017/0362692 2017.
- 14. Gandhi AS, Levi CG. Phase selection in precursor-derived yttrium aluminum garnet and related Al₂O₃-Y₂O₃ compositions. J Mater Res. 2005;20(4):1017-25. https://doi.org/10.1557/ JMR.2005.0133
- 15. Godbole E, von der Handt A, Poerschke D. Apatite and garnet stability in the Al-Ca-Mg-Si-(Gd/Y/Yb)-O systems and implications for T/EBC: CMAS reactions. J Am Ceram Soc. 2022;105(2):1596-609. https://doi.org/10.1111/jace.18179
- 16. German RM. Sintering trajectories: description on how density, surface area, and grain size change. JOM. 2016;68:878-84. https://doi.org/10.1007/s11837-015-1795-8
- 17. Padture NP, Klemens PG. Low thermal conductivity in garnets. J Am Ceram Soc. 1997;80(4):1018-20. https://doi.org/10.1111/j. 1151-2916.1997.tb02937.x
- 18. Su Y, Trice R, Faber K, Wang H, Porter W. Thermal conductivity, phase stability, and oxidation resistance of Y₃Al₅O₁₂ (YAG)/Y₂O₃-ZrO₂ (YSZ) thermal-barrier coatings. Oxid Met. 2004;61(3):253-71. https://doi.org/10.1023/B:OXID.0000025334. 02788.d3
- 19. Sakaguchi I, Haneda H, Tanaka J, Yanagitani T. Effect of composition on the oxygen tracer diffusion in transparent

- vttrium aluminium garnet (YAG) ceramics. J Am Ceram Soc. 1996;79(6):1627-32. https://doi.org/10.1111/j.1151-2916
- 20. Gell M, Wang J, Kumar R, Roth J, Jiang C, Jordan EH. Higher temperature thermal barrier coatings with the combined use of yttrium aluminum garnet and the solution precursor plasma spray process. J Therm Spray Technol. 2018;27(4):543-55. https:// doi.org/10.1007/s11666-018-0701-7
- 21. Yu Y-C, Poerschke DL. Design of thermal and environmental barrier coatings for Nb-based alloys for high-temperature operation. Surf Coat Technol. 2022;431:128007. https://doi.org/ 10.1016/i.surfcoat.2021.128007
- 22. Schmitt MP, Stokes JL, Rai AK, Schwartz AJ, Wolfe DE. Durable aluminate toughened zirconate composite thermal barrier coating (TBC) materials for high temperature operation. J Am Ceram Soc. 2019;102(8):4781–93. https://doi.org/10.1111/jace.
- 23. Turcer LR, Krause AR, Garces HF, Zhang L, Padture NP. Environmental-barrier coating ceramics for resistance against attack by molten calcia-magnesia-aluminosilicate (CMAS) glass: Part I, YAlO₃ and γ -Y₂Si₂O₇. J Eur Ceram Soc. 2018;38(11):3905-13. https://doi.org/10.1016/j.jeurceramsoc. 2018.03.021
- 24. Poerschke DL, Jackson RW, Levi CG. Silicate deposit degradation of engineered coatings in gas turbines: progress toward models and materials solutions. Annu Rev Mater Res. 2017;47:297-330. https://doi.org/10.1146/annurev-matsci-010917-105000

How to cite this article: Yu Y-C, Godbole EP, Berrios J, Hewage N, Poerschke DL. Slow sintering in garnet-containing Y and Gd zirconate-aluminate mixtures for thermal barrier coatings. J Am Ceram Soc. 2023;106:4519-4525.

https://doi.org/10.1111/jace.19121